ACS APPLIED MATERIALS & INTERFACES

www.acsami.org Research Article

Scavenger-Supported Photocatalytic Evidence of an Extended Type I Electronic Structure of the TiO_2@Fe_2O_3 Interface

Anita Trenczek-Zajac,* Milena Synowiec,* Katarzyna Zakrzewska, Karolina Zazakowny, Kazimierz Kowalski, Andrzej Dziedzic, and Marta Radecka

Cite This: *ACS Appl. Mater. Interfaces* 2022, 14, 38255−38269 Read Online

ACCESS | Metrics & More | Article Recommendations | Supporting Information

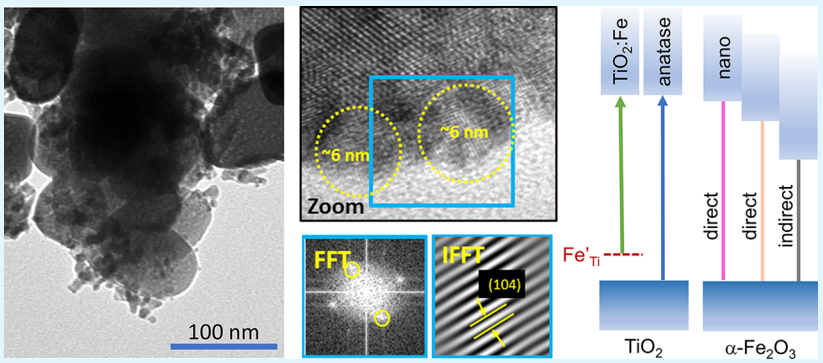

ABSTRACT: Heterostructures of TiO_2@Fe_2O_3 with a specific electronic structure and morphology enable us to control the interfacial charge transport necessary for their efficient photocatalytic performance. In spite of the extensive research, there still remains a profound ambiguity as far as the band alignment at the interface of TiO_2@Fe_2O_3 is concerned. In this work, the extended type I heterojunction between anatase TiO_2 nanocrystals and α-Fe_2O_3 hematite nanograins is proposed. Experimental evidence supporting this conclusion is based on direct measurements such as optical spectroscopy, X-ray photoemission spectroscopy, scanning electron microscopy, high-resolution transmission electron microscopy (HRTEM), and the results of indirect studies of photocatalytic decomposition of rhodamine B (RhB) with selected scavengers of various active species of $OH^{\bullet}$, $h^{\bullet}$, e^{-}, and $^{\bullet}O_2^{-}$. The presence of small 6−8 nm Fe_2O_3 crystallites at the surface of TiO_2 has been confirmed in HRTEM images. Irregular 15−50 nm needle-like hematite grains could be observed in scanning electron micrographs. Substitutional incorporation of Fe^{3+} ions into the TiO_2 crystal lattice is predicted by a 0.16% decrease in lattice parameter a and a 0.08% change of c, as well as by a shift of the Raman $E_{g(1)}$ peak from 143 cm^{-1} in pure TiO_2 to 149 cm^{-1} in Fe_2O_3-modified TiO_2. Analysis of O 1s XPS spectra corroborates this conclusion, indicating the formation of oxygen vacancies at the surface of titanium(IV) oxide. The presence of the Fe^{3+} impurity level in the forbidden band gap of TiO_2 is revealed by the 2.80 eV optical transition. The size effect is responsible for the absorption feature appearing at 2.48 eV. Increased photocatalytic activity within the visible range suggests that the electron transfer involves high energy levels of Fe_2O_3. Well-programed experiments with scavengers allow us to eliminate the less probable mechanisms of RhB photodecomposition and propose a band diagram of the TiO_2@Fe_2O_3 heterojunction.

KEYWORDS: *TiO_2, Fe_2O_3, heterostructures, band diagram, interface, electron transfer, photocatalysis*

1. INTRODUCTION

Although anatase TiO_2 and hematite Fe_2O_3 have been studied for many years, completely new effects arise when the combination of both oxides is used in catalysis,[1] photocatalysis,[2−6] Li-ion batteries,[7,8] gas sensors,[9,10] and photoelectrochemical water splitting to generate green hydrogen.[11−13] When treated separately, each of the metal oxides mentioned above offers many attractive features but suffers from fundamental drawbacks as well.

Titanium dioxide is one of the semiconductors that are the most frequently encountered in photocatalysis,[14] solar cells,[15] self-cleaning coatings,[16] and gas sensors[17] due to its nontoxicity, chemical stability, abundance, and low cost. Nevertheless, its basic disadvantage is a wide band gap E_g of above 3.0 eV, resulting in high transparency to the visible range of the light spectrum. Numerous attempts have been made to engineer the TiO_2 band gap with the aim of reducing the

Received: April 19, 2022
Accepted: July 21, 2022
Published: August 15, 2022

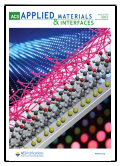

separation between the edges of the valence and conduction bands or creating additional states in the forbidden band gap. However, the problem of better adaptation of the optical absorption of TiO_2 to the spectrum of the Sun has never found a satisfactory solution. All efforts, including doping, largely failed due to the development of undesirable recombination centers, inherent to this method of band gap modification.

In contrast to TiO_2, hematite Fe_2O_3 is a good representative of narrow-band-gap semiconductors (2.2 eV). Its absorption spectrum allows for efficient light harvesting within the visible range. Similarly to TiO_2, it is inexpensive and environmentally friendly.[18,19] However, fast recombination of charge carriers resulting from extremely short lifetimes of electron−hole pairs (<10 ps) and small diffusion lengths of holes (2−4 nm) inevitably contributes to the degradation of photocatalytic performance and the low efficiency of energy conversion processes. The low mobility of minority charge carriers and their limited diffusion length are considered responsible for the high surface and bulk recombination rates of charge carriers.[20] Therefore, the biggest challenge is to restrict the recombination of the photoexcited electron and holes in order to extend their lifetime to drive much slower photocatalytic processes at the surfaces and interfaces. One of the most efficient solutions to this problem is the creation of solid-state junctions.[21]

Metal oxide heterojunctions can be categorized into type I, II, and III depending on how the band edges of two semiconductors relate to one another.[22] Moreover, different charge carrier transfer routes have been proposed, among which Z and S schemes are the most popular.[22,23]

To take advantage of the best features of both oxides, TiO_2@Fe_2O_3 heterostructures have been studied as an alternative to improve the photocatalytic performance due to charge transfer phenomena across the interfaces.[8,24−26] Control over interfacial electronic transport is widely accepted as necessary to provide efficient operation of devices based on materials that contain numerous heterojunctions. However, to ensure the best photocatalytic decomposition of organic compounds, the type and electronic structure of the heterojunctions must be controlled as well as their morphology.

In fact, in the case of TiO_2@Fe_2O_3, there remains a profound ambiguity as far as the electronic structure and its type is concerned.[27−29] One can find different models of the configuration of electronic bands that consequently predict various mechanisms of electron and hole separation.[21] Research results in favor of the type I[27,30−33] and type II[19,28,34−36] or that of the extended type I have been published.[4,29,37,38]

Formation of a type I heterojunction, where the conduction band (CB) edge of TiO_2 is above the CB of Fe_2O_3 and the valence band (VB) edge of TiO_2 is below that of Fe_2O_3, has been proposed.[27,30−32] However, in this case, the photoelectrons and photoholes generated in TiO_2 upon UV radiation would transfer to the conduction and valence bands of Fe_2O_3, respectively, with no improvement toward suppression of the charge recombination. On the other hand, there are studies[19,28,34−36] that conclude that a type II heterojunction is created, where electrons formed under visible light in Fe_2O_3 can be transferred to the CB of TiO_2.[39] However, there are also reports[4,29,37,38] in which it is accepted that although the TiO_2@Fe_2O_3 composite forms type I heterojunctions, it behaves favorably with respect to electron transfer. It is claimed that in $CB_{Fe_2O_3}$, higher levels exist to which the electrons can be transported. Higher levels in iron III oxide are located above CB_{TiO_2}, so excited e^- can be injected to titanium dioxide. It should be mentioned that the type of band alignment in TiO_2@Fe_2O_3 has not been elucidated based on the direct experiments concerning the heterostructures. UV−vis spectroscopy, VB X-ray photoemission spectroscopy (XPS), and work function measurements as well as photocatalysis have been carried out individually on TiO_2 and Fe_2O_3. Therefore, the knowledge of the relative positions of the valence and conduction bands of these two materials is not explicitly supported by the experimental results.[30,35,38]

Most of the studies[2−6] on the photocatalytic behavior of heterostructures aim to improve the photodegradation rate. For example, Xia et al.[2] studied core−shell α-Fe_2O_3@TiO_2 nanocomposites prepared by the heteroepitaxial growth route and showed their improved photocatalytic activity toward the decomposition of rhodamine B (RhB) in the visible light region. Yao et al.[3] have designed and fabricated Fe_2O_3−TiO_2 core−shell nanorod arrays using the glancing angle deposition technique (GLAD). These arrays have been shown to be more efficient for the degradation of methylene blue and the conversion of CO_2 under visible light illumination. Li et al.[4] synthesized dendritic α-Fe_2O_3/TiO_2 nanocomposites for visible light degradation of eosin red, Congo red, methylene blue, and methyl orange. Huang et al.[29] demonstrated enhanced photocatalytic denitrification of pyridine over TiO_2/α-Fe_2O_3 nanocomposites under visible light irradiation. Mendiola-Alvarez et al.[5] proposed a new P-doped Fe_2O_3−TiO_2 mixed oxide prepared by a microwave-assisted sol gel method for the photocatalytic degradation of sulfamethazine (SMTZ) with better efficiency within the visible range of the electromagnetic spectrum than that of unmodified Fe_2O_3−TiO_2 and TiO_2. Wannapop et al.[6] studied the photocatalytic degradation of RhB on 1D TiO_2 nanorods synthesized by the hydrothermal method and decorated with Fe_2O_3. The level of degradation after 5 h increased from 30% for TiO_2 to 63% for the Fe_2O_3/TiO_2 heterostructure due to favorable charge transfer at the interface.

However, improvement in the photocatalytic activity is only the secondary aim of our current research. Determination of the type of the electronic structure of TiO_2@Fe_2O_3 should be considered as the primary motivation for this work. The novelty is based on the particular approach to this task, which consists in the application of photocatalysis with specific scavengers of $OH^•$, $h^•$, e^-, and $^•O_2^-$ as an experimental tool to draw conclusions regarding the CB and VB edge configuration.

In our previous paper,[33] we have proposed the formation of an intermediate layer of TiO_2:Fe as a consequence of Fe_2O_3 deposition on the surface of the TiO_2 nanocrystal. The incorporation of Fe^{3+} ions into the TiO_2 lattice is associated with the appearance of an additional acceptor level within the TiO_2 band gap.

In this work, the interface of a specific morphology has been engineered, and the correlation between morphological properties and electronic structure has been demonstrated for the first time. Direct measurements, such as optical spectroscopy, XPS, scanning electron microscopy (SEM), and high-resolution transmission electron microscopy (HRTEM), allowed us to draw conclusions regarding the electronic structure of the interface and its morphology. In addition, indirect studies based on the decomposition of the classical

https://doi.org/10.1021/acsami.2c06404
ACS Appl. Mater. Interfaces 2022, 14, 38255−38269

Table 1. Detailed Conditions of Material Preparation

sample	$Fe(NO_3)_3$[a]/TiO_2 ratio ±0.2 [mL/g]	Fe/(Fe + Ti) at. ratio [%]	
		assumed	from EDX analysis
TiO_2			
TiO_2@0.2%Fe_2O_3	3.46	0.239	0.61(2)
TiO_2@1%Fe_2O_3	15.57	1.066	1.23(2)
TiO_2@2%Fe_2O_3	34.60	2.339	3.28(2) (4.09(3))[b]
TiO_2@10%Fe_2O_3	155.70	9.727	10.81(4)
TiO_2@20%Fe_2O_3	346.00	19.320	25.49(4) (24.40(3))[b]

[a]$Fe(NO_3)_3$ concentration: 8.665(4)·10^{-3} M, $(NH_4)_2CO_3$—saturated solution—100 mL per 1.000(1) g of TiO_2. [b]The atomic Fe/(Fe + Ti) ratio [%] based on the XPS analysis.

RhB model dye by TiO_2@Fe_2O_3 nanocrystals with and without selected scavengers of various active species have been carried out. A logical scheme has been proposed to eliminate the least probable decomposition routes. Knowledge of the possible mechanism of decomposition of a specific dye is believed to assist in drawing conclusions regarding the charge transfer mechanism at the TiO_2@Fe_2O_3 interface.

2. EXPERIMENTAL SECTION

2.1. Synthesis of TiO_2 Nanocrystals. A detailed description of the growth process of anatase nanocrystals has been presented in our previous article.[33] Briefly, the hydrothermal method was used to synthesize TiO_2 nanocrystals as a mixture of cubes and rods. Titanium tetraisopropoxide played the role of a titanium dioxide precursor, and diethanolamine acted as a shape-controlling agent. The prepared solution was heated to 215 °C for 24 h in a stainless-steel autoclave. The resulting precipitate was washed with 0.1 M HCl, distilled water, and ethanol and then dried and calcined at 500 °C for 3 h.

2.2. Formation of TiO_2@Fe_2O_3 Heterojunctions. The preparation conditions for particular TiO_2@Fe_2O_3 heterojunctions are given in Table 1. Typically, as described for the TiO_2@2%Fe_2O_3 sample, 75 ml of ammonium carbonate was poured into the beaker containing 0.75 g of TiO_2 anatase nanocrystals. During continuous stirring, 25.95 mL of iron(III) nitrate was added dropwise. Then, the temperature of the solution was increased to 70 °C to decompose ammonium carbonate into NH_3, CO_2, and H_2O. After 4 h, the beaker was covered with a watch glass and placed in the dryer for 18 h at 70 °C to complete the decomposition process. The ammonia formed during heating caused the pH of the mixture to increase, and an alkaline environment was obtained, resulting in the precipitation of iron(III) hydroxide $Fe(OH)_3$. The nanopowder was then collected by centrifugation and washed five times with a 0.5 %vol ammonia solution. The freshly prepared nanopowder was dispersed in isopropyl alcohol and dried at 70 °C for complete alcohol evaporation. To transform $Fe(OH)_3$ deposited on the TiO_2 surface into Fe_2O_3, it was necessary to carry out the calcination process at 500 °C for 2 h.

2.3. Characterization. X-ray diffraction (XRD) was used to study the crystal structure of the obtained materials. Measurements were carried out within the 2θ range from 20 to 80° using an X'PertPro PANalytical diffractometer (Philips) equipped with a copper anode as a radiation source ($K_{\alpha 1}$ = 0.15406 nm). The HighScore Plus software and the PDF-2 database were applied for qualitative analysis. Quantitative analysis was performed using the Rietveld method. Supplementary conclusions concerning the phase structure were drawn on the basis of Raman spectroscopy. The Jobin-Yvon LabRam HR800 spectrometer, featuring a green laser (532 nm) and a diffraction grating of 1800 g/mm, was applied. The spectra were collected in a range of 1/λ from 80 to 800 cm^{-1}. A scanning electron microscope (Nova NanoSEM 200) equipped with an energy-dispersive X-ray (EDX) detector was used to calculate the Fe/(Fe + Ti) concentration. Furthermore, transmission electron microscopy (TEM) and HRTEM images were obtained using JEOL JEM-1011 and FEI Tecnai microscopes at accelerating voltages of 100 kV and 200 kV, respectively. Bright-field and high-angle annular dark-field scanning transmission electron microscopy (HAADF STEM) images were obtained in conjunction with EDX spectrum mapping to gain information on the microstructure of the TiO_2 and TiO_2@Fe_2O_3 materials. Digital Micrograph software was employed for analyzing the HRTEM images using fast Fourier transform (FFT) and inverse fast Fourier transform (IFFT) techniques, which allowed us to calculate the interplanar spacing of the observed phases.

The optical properties were determined from the total reflectance spectra $R_{tot}(\lambda)$ recorded within the wavelength range of 220−2200 nm using the JASCO V-670 UV−VIS−NIR spectrophotometer equipped with an integrating sphere of 150 nm diameter. The energies of the optical transitions were established as corresponding to the maxima of a wavelength derivative $dR_{tot}/d\lambda$ of the total reflectance coefficient with an uncertainty of 0.02 eV.

The chemical composition and electronic state of the ions at the surface were determined by XPS using a VSW spectrometer (Vacuum Systems Workshop Ltd.) with Al Kα radiation. The atomic ratio C_x of an element x on the surface was calculated as $C_x = \frac{A_x / S_x}{\sum_i A_x / S_x}$ where A_x represents the peak area of element x and S_x is the normalized sensitivity for photoelectrons (S_{Ti} = 4.95 and S_{Fe} = 10.86).

2.4. Photocatalytic Activity. The photocatalytic activity toward the decomposition of RhB was studied under visible light (12 Philips TL 8W/54−7656 bulb lamps) for all materials obtained. Under typical conditions, 0.075 g of the photocatalyst was dispersed in 50 mL of RhB solution (5 × 10^{-5} M). In some experiments, 1 mL of H_2O_2 (30%) was added to the solution and subjected to 30 min of stirring in the dark to achieve an equilibrium of adsorption−desorption, and 2 ml of the solution was collected and filtered. After a given time interval, other portions of the previously illuminated solution were removed and filtered. The UV−vis−NIR spectrophotometer, JASCO V-670, was used to measure the absorbance of the samples over the range 400−800 nm. Finally, the C/C_o ratio was calculated, where C is the concentration of RhB after a certain time of photocatalysis and C_o is the initial concentration of RhB determined for a wavelength equal to 554 nm.

To investigate the active species generated in the photocatalytic system (PS) consisting of a photocatalyst, RhB, and H_2O_2, scavenger experiments were performed. Ethylenediaminetetraacetic acid (EDTA-2Na, 10 mM), benzoquinone (p-BQ, 1 mM), $AgNO_3$ (100 mM), and *tert*-butyl alcohol (t-BuOH) (1:20 vol.) were used as scavengers introduced into the PS in the amount of 1 ml to capture holes ($h^•$), superoxide radicals ($^•O_2^-$), electrons (e^-), and hydroxyl radicals ($OH^•$), respectively.

Tests of cyclic photocatalysis were carried out using TiO_2@0.2% Fe_2O_3 and TiO_2@2%Fe_2O_3 heterostructures. After dark adsorption, a 90 min photocatalytic decomposition process of RhB was carried out and repeated four times. After each decomposition process, the photocatalyst was separated from the solution of RhB by centrifugation and washed with ethanol three times. After that, the powder was dried for 4 h at 70 °C and used again.

3. RESULTS

3.1. Crystal Structure and Morphology. The presence of iron in the heterostructures was confirmed by EDX analysis

https://doi.org/10.1021/acsami.2c06404
ACS Appl. Mater. Interfaces 2022, 14, 38255−38269

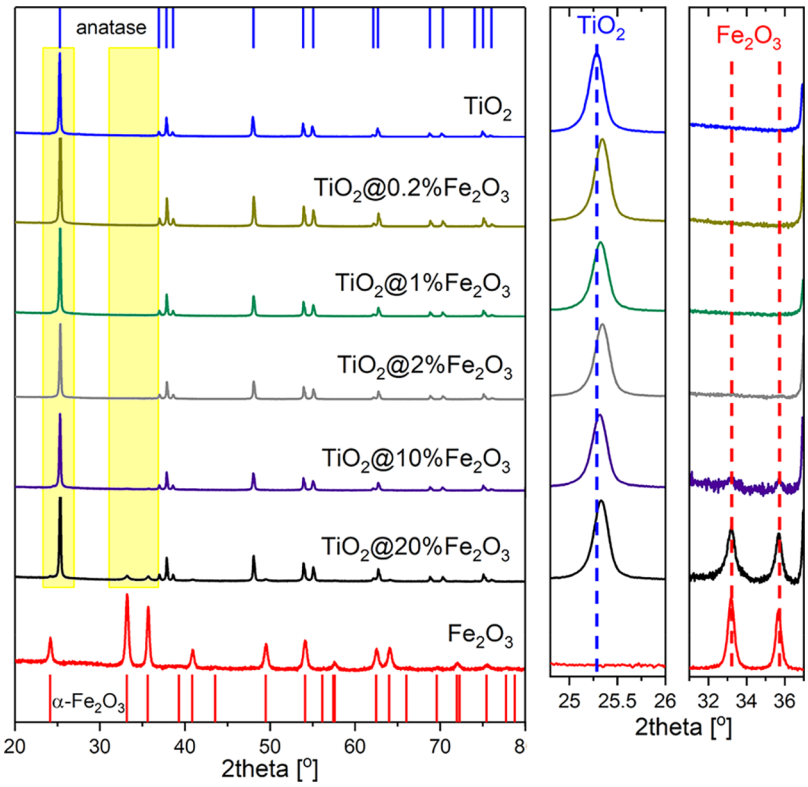

Figure 1. XRD patterns of TiO_2 nanocrystals and TiO_2 nanocrystals covered with Fe_2O_3. The top bars represent the positions of the anatase peaks, while the bottom bars correspond to α-Fe_2O_3.

(Figure S1a), and the iron contents are shown in Table 1. The crystal structure has been identified on the basis of XRD data and the use of the PDF-2 database. Analysis has shown that TiO_2 nanocrystals are single-phase and crystallize in a structure of anatase (JCPDS-ICDD #03-065-5714) (Figure 1) or contain traces of rutile (Figure S1b). In the case of Fe_2O_3, all peaks have been assigned to hematite α-Fe_2O_3 (JCPDS-ICDD #01-073-2234). For TiO_2@Fe_2O_3, the presence of secondary phase α-Fe_2O_3 has been confirmed only at the highest concentration of Fe^{3+} ions during preparation. At lower concentrations of Fe^{3+} ions, XRD has not revealed any evidence for the crystallization of iron oxides. Representative XRD patterns are included in Figure 1.

Depending on the electronegativity and ionic radius, metal ions can build into oxides either interstitionally or substitutionally. The ionic radius of the Fe^{3+} ion is equal to 0.064 nm and is slightly smaller than that of Ti^{4+} ion—0.068 nm, while the Pauling electronegativities of Fe^{3+} (1.83) and Ti^{4+} (1.54) are similar. It is, thus, likely that Fe^{3+} ions substitutionally occupy cationic Ti^{4+} sites in the TiO_2 lattice.[40] A distortion of the lattice would manifest itself by a decrease in the lattice parameters. As a result, the positions of all TiO_2:Fe diffraction peaks should shift to higher diffraction angles. This effect can be observed in the XRD pattern of TiO_2@20%Fe_2O_3 compared to that of TiO_2. On the basis of Rietveld analysis, the parameters of the unit cell have been calculated and found to be equal to $a = b = 0.3791(1)$ nm, $c = 0.9515(1)$ nm for TiO_2 and $a = b = 0.3785(1)$ nm, $c = 0.9507(1)$ nm for TiO_2@20%Fe_2O_3. The relative decrease in lattice parameter a is equal to 0.16% while that of parameter c is about 0.08%. This change indicates the incorporation of Fe^{3+} ions into the cationic sublattice of anatase.[33]

The Raman spectra of the TiO_2, TiO_2@Fe_2O_3, and Fe_2O_3 nanocrystals are shown in Figure 2. A typical spectrum

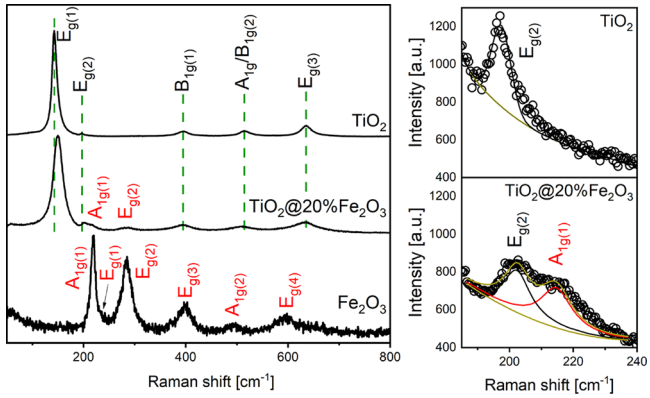

Figure 2. Raman spectra of TiO_2, TiO_2@Fe_2O_3, and Fe_2O_3 nanomaterials.

composed of five bands is observed for anatase TiO_2, while that of α-Fe_2O_3 contains six well-developed bands.[41−43] The positions of all Raman peaks are given in Table 2.

When considering TiO_2@Fe_2O_3, in addition to the bands that can be attributed to anatase, two surplus bands can be seen. The Raman shift corresponding to 213−223 cm^{-1} is attributed to α-Fe_2O_3 $A_{1g(1)}$.[42,43] Another band appearing at 284 cm^{-1} can be attributed α-Fe_2O_3 $E_{g(2)}$.[41−43] Substitutional incorporation of Fe^{+3} ions for Ti^{+4} cations, as determined by XRD data, is further supported by the change of the $E_{g(1)}$ band from 143 cm^{-1} (TiO_2 nanocrystals) to 149 cm^{-1} (TiO_2@20% Fe_2O_3) with simultaneous reduction of band intensity by 79%, as shown in Table 2. It has been suggested[44] that the shift in

https://doi.org/10.1021/acsami.2c06404
ACS Appl. Mater. Interfaces 2022, 14, 38255−38269

Table 2. Raman Shift and Intensity of the Selected Bands for TiO_2, Fe_2O_3, and TiO_2@20%Fe_2O_3 Nanomaterials

	$E_{g(1)}$ of TiO_2		$A_{1g(1)}$ of Fe_2O_3		$E_{g(2)}$ of Fe_2O_3	
sample	Raman shift [cm^{-1}]	intensity [a.u.]	Raman shift [cm^{-1}]	intensity [a.u.]	Raman shift [cm^{-1}]	intensity [a.u.]
TiO_2	143(1)	29041(5)				
TiO_2@20%Fe_2O_3	149(1)	6026(1)	214(1)	211(1)	284(1)	134(1)
Fe_2O_3			218(1)	177(1)	284(1)	131(1)

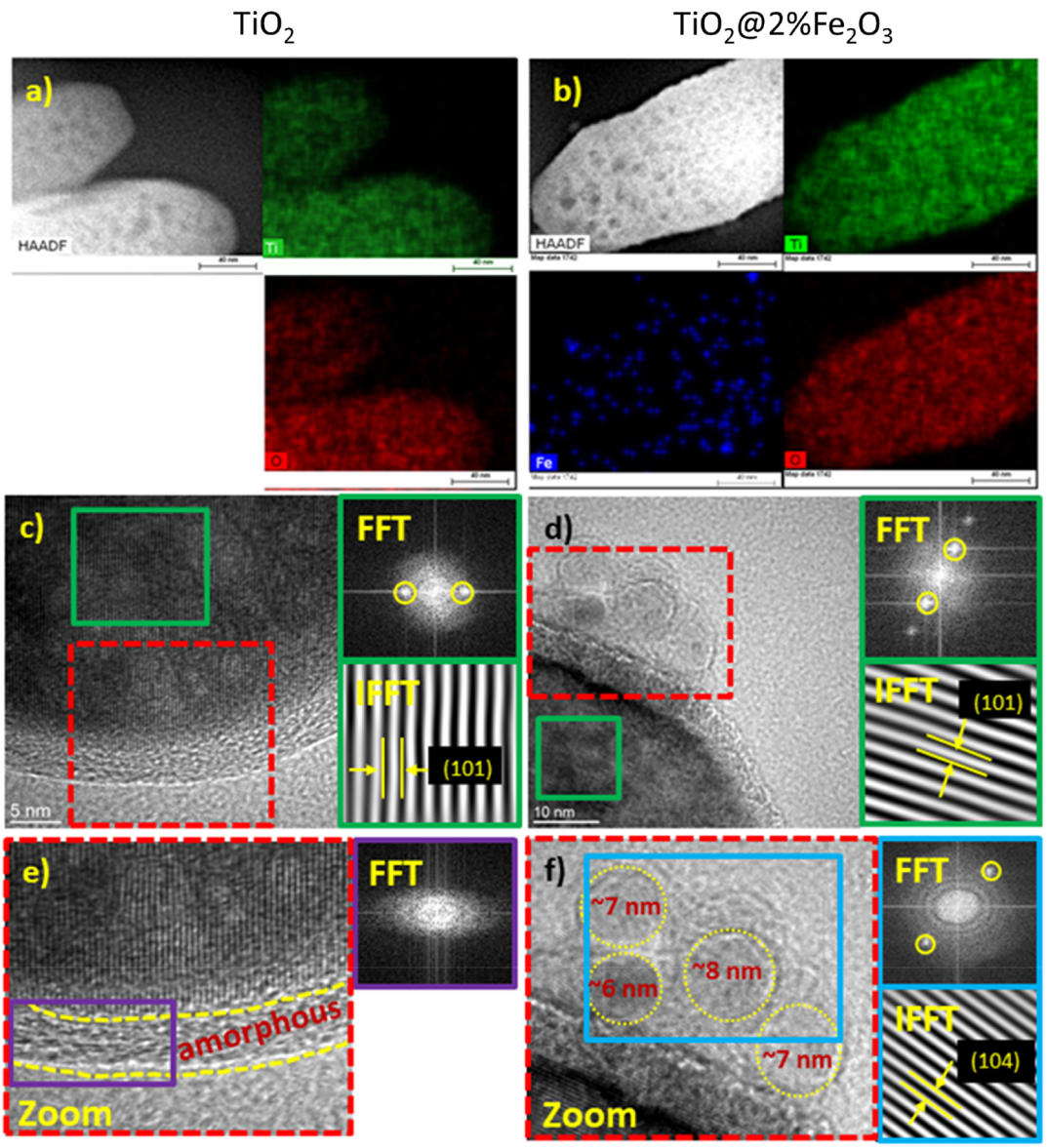

Figure 3. (a,b) EDX mapping images; (c,d) HRTEM images with FFT and IFFT analyses indicate the existence of the (101) plane of anatase TiO_2; (e,f) FFT of the purple/blue rectangle of the zoomed-in area shows an amorphous coating (TiO_2) or hematite nanoparticles of size 6−8 nm in the (104) plane of α-Fe_2O_3 (TiO_2@2%Fe_2O_3).

the anatase $E_{g(1)}$ Raman band is the result of lattice defects. TiO_2 doping with iron(III) ions was postulated in our previous paper[33] based on the spectrophotometric data.

TEM images provided information on the shape and size of the particles (Figure S2). Titanium dioxide nanocrystals form elongated rods ca. 230 nm long (Figure S2a). The analysis of TiO_2@Fe_2O_3 indicates that Fe_2O_3 forms a discontinuous layer of nanograins with a size of 15−50 nm at the surface of the TiO_2 nanocrystals (Figure S2b,c). In the case of TiO_2@2% Fe_2O_3, Fe_2O_3 crystals take a needle-like shape and grow only on certain walls of TiO_2 (Figure S2b).

EDX mapping and analysis of HRTEM images are shown in Figure 3. All IFFT calculations were performed after noise reduction using spots marked with a yellow circle in the FFT patterns. Then, masking was applied, and the resulting IFFT images presented the arrangement of crystallographic planes (black lines), which allowed the measurement of interplanar spacing.

EDX spectrum mapping of the regions shown in HAADF STEM images (Figure 3a,b) was used to create maps of Ti, O, and Fe elements. These results reveal that in the case of TiO_2@2%Fe_2O_3, iron is distributed homogeneously (Figure

https://doi.org/10.1021/acsami.2c06404
ACS Appl. Mater. Interfaces 2022, 14, 38255−38269

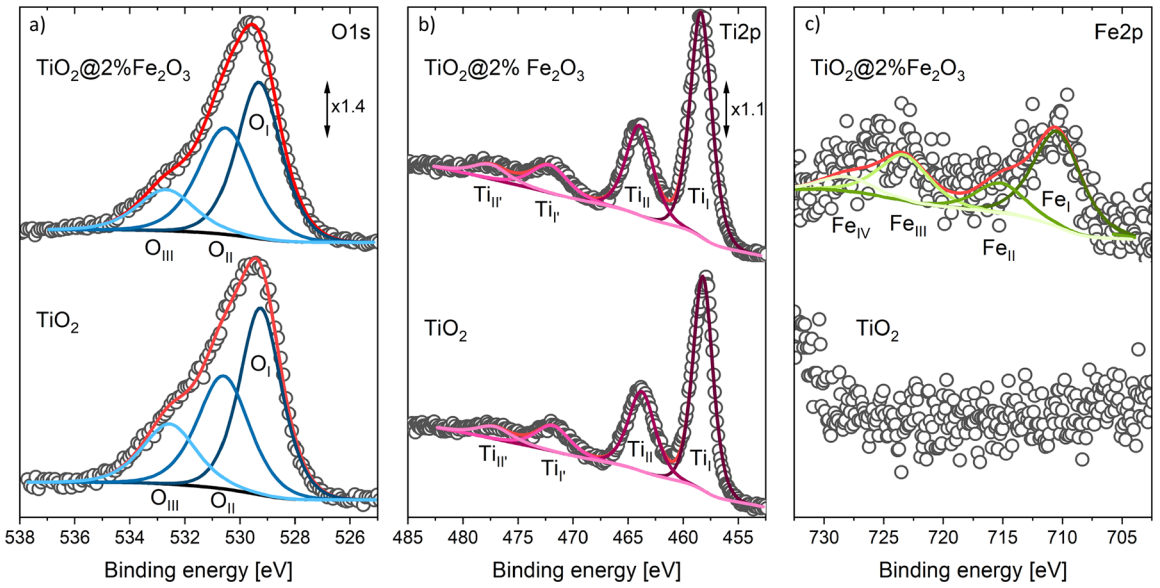

Figure 4. Deconvolution of the O1s, Ti2p, and Fe2p XPS spectra of TiO_2 and TiO_2@2%Fe_2O_3 nanocrystals.

Table 3. Results of XPS Analysis of TiO_2 and TiO_2@2%Fe_2O_3 Nanocrystals—Assignment of Ti2p, O1s, and Fe2p peaks to Certain Types of Bonding

	binding energy (eV)			
symbol	TiO_2	TiO_2@2%Fe_2O_3	type of bonding	refs
		Ti2p		
Ti_I	458.2(3)	458.4(3)	Ti $2p_{3/2}$, O−Ti−O	[45]
Ti_{II}	463.8(3)	464.0(3)	Ti $2p_{1/2}$, O−Ti−O	[45]
$Ti_{I'}$	472.1(3)	472.2(3)	satellite of Ti$2p_{3/2}$, O−Ti−O	[45]
$TiI_{I'}$	477.3(3)	477.6(3)	satellite of Ti$2p_{1/2}$, O−Ti−O	[45]
		O1s		
O_I	529.3(4)	529.3(4)	Ti−O−Ti	[46]
O_{II}	530.6(4)	530.6(4)	oxygen vacancies or defects	[46]
O_{III}	532.7(4)	532.7(4)	chemisorbed species, e.g., OH^-, H_2O, O^{2-}	[46]
		Fe2p		
Fe_I		710.6(7)	Fe $2p_{3/2}$, Fe^{3+} in Fe_2O_3	[47, 49]
Fe_{II}		715.2(8)	satellite of Fe $2p_{3/2}$, Fe^{3+} in Fe_2O_3	[47, 49]
Fe_{III}		723.5(7)	Fe $2p_{1/2}$, Fe^{3+} in Fe_2O_3	[47, 49]
Fe_{IV}		728.4(7)	satellite of Fe $2p_{1/2}$, Fe^{3+} in Fe_2O_3	[47, 49]

3b), and for the TiO_2@20%Fe_2O_3 sample, Fe_2O_3 grains of size tens of nanometers are also observed (Figure S3a).

Well-crystallized structures can be observed for all synthesized powders that are represented by the distinct spots on the FFT patterns. The green rectangles in Figures 3c,d, and S3b indicate the investigated area, the ROI (region of interest) of the FFT analysis. In each case, the spots obtained from the ROI correspond to an interplanar spacing of about 0.354 nm, which is well-correlated with the {101} plane of anatase TiO_2, the presence of which is also confirmed by XRD studies. However, the amorphous layer that was a part of the rod was observed at the surface of the TiO_2 nanocrystals (Figure 3e). Furthermore, in the HRTEM images of the TiO_2@2%Fe_2O_3 and TiO_2@20%Fe_2O_3 composites (Figures 3f and S3c), nanograins of size 6−8 nm deposited on the surface of the TiO_2 nanocrystals were found. To investigate their crystal structure, we performed the FFT analysis from the area in the blue rectangle, and then, the reverse FFT analysis was executed. The measured interplanar spacing was equal to 0.273 nm, which is close to the 0.270 nm lattice spacing of the {104} crystal planes of hematite.

3.2. Electronic Structure. The electronic structure of the components of the composite materials, such as TiO_2@Fe_2O_3, studied by XPS and optical spectrophotometry, plays a special role in the prediction of the character and type of the interface. Additional information about the interfacial charge transfer processes can be obtained from the carefully designed photocatalytic experiment. In this work, we have carried out a series of tests aimed at the photocatalytic degradation of the standard dye, that is, RhB, with and without certain scavengers. From the rates of decomposition of dye, conclusions about the probabilities of charge transfer processes can be drawn, which helps figure out the electronic structure of the interface.

Surface chemistry of the selected elements: Ti, O, and Fe, as well as surface defects, were studied by means of XPS. Figure 4 shows the high-resolution spectra of O1s, Ti2p, and Fe2p from the TiO_2 and TiO_2@2%Fe_2O_3 nanocrystals. XPS data concerning TiO_2@20%Fe_2O_3 nanocrystals with the highest amount of Fe_2O_3 are presented in Figure S4. The values of all

https://doi.org/10.1021/acsami.2c06404
ACS Appl. Mater. Interfaces 2022, 14, 38255−38269

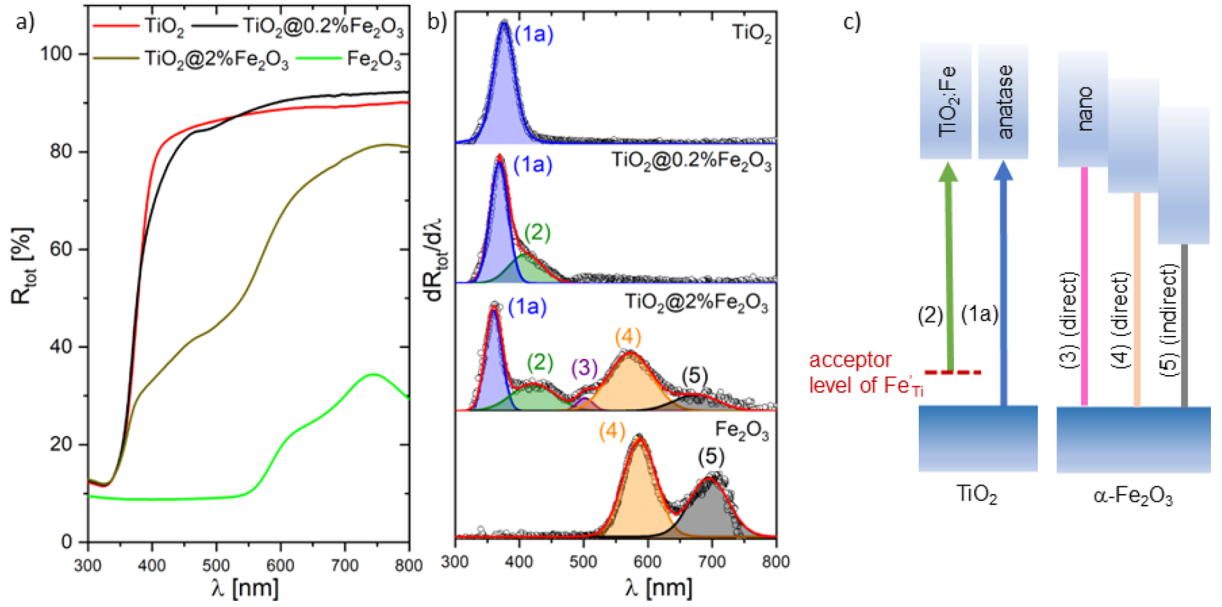

Figure 5. (a) Spectral dependence of the total optical reflectance R_{tot}, (b) first derivative spectra $dR_{tot}/d\lambda$ of TiO_2@Fe_2O_3; $h\nu$—photon energy, and (c) diagrams of optical transitions in TiO_2 and α-Fe_2O_3.

binding energies determined by the fitting of the different XPS lines are given in Tables 3 and S1.

The shape of the Ti2p XPS peak is complex in all samples. In the case of TiO_2, four components with the following binding energies 458.2 eV (Ti_I), 463.8 eV (Ti_{II}), 472.1 eV ($Ti_{I'}$), and 477.3 eV ($Ti_{II'}$) were fitted. The $Ti2p_{3/2}$−$Ti2p_{1/2}$ (Ti_I−Ti_{II}) doublet arises from spin orbit splitting and can be ascribed to Ti^{4+} ions in TiO_2 (titanium−oxygen−titanium bonding). The higher energies of 472.1 eV ($Ti_{I'}$) and 477.3 eV ($Ti_{II'}$) correspond to the satellite peaks of $Ti2p_{3/2}$ and $Ti2p_{1/2}$, respectively.[45] Upon covering TiO_2 nanocrystals with Fe_2O_3, the Ti2p XPS peaks shift slightly toward higher binding energies, and their exact positions depend on the amount of deposited Fe_2O_3, that is, the shift of 0.1−0.3 eV is observed at the lower amount of Fe_2O_3 (TiO_2@2%Fe_2O_3) while that of 0.6−1.0 eV at the higher amount of Fe_2O_3 (TiO_2@20% Fe_2O_3). The shift of these peaks indicates changes in the chemical environment of Ti^{4+} ions.

Analysis of the O1s peak reveals three components at 529.3 eV (O_I), 530.6 eV (O_{II}), and 532.7 eV (O_{III}). The lowest-energy O_I component is related to lattice oxygen O^{2-} in a fully coordinated position in the TiO_2 lattice (titanium−oxygen−titanium bonding). The highest-energy O_{III} component is associated with species, such as hydroxyl groups OH^-, water molecules H_2O, or dissociated oxygen O^{2-}, chemisorbed at the surface. The medium-energy O_{II} component, in agreement with reports in the literature,[46] can be attributed to the oxygen vacancy V_O in the titanium dioxide lattice. It should be noted that a small amount of Fe_2O_3 on the surface of TiO_2 does not cause any changes to the positions of the O1s peaks, while its high amount causes a shift of about 0.1−0.2 eV toward higher binding energies (Figure S4).

The Fe2p XPS peak has been fitted with four lines. In the case of TiO_2@2%Fe_2O_3, they are located at 710.6 eV (Fe_I), 715.2 eV (Fe_{II}), 723.5 eV (Fe_{III}), and 728.4 eV (Fe_{IV}). Two main Fe_I and Fe_{III} peaks correspond to $Fe2p_{3/2}$ and $Fe2p_{1/2}$ states, respectively, which shows that iron is present in the form of Fe^{3+} ions. The component denoted Fe_{II} has been assigned to the satellite of $Fe2p_{3/2}$ and to the satellite of $Fe2p_{1/2}$.[47−49] At the highest amount of Fe_2O_3, not only an increased intensity of these peaks is observed but a shift of about 0.4−0.8 eV toward higher binding energies can also be seen (Figure S4). Quantitative analysis of XPS data indicates that the atomic fraction of iron reaches 4.1% in the case of lower (TiO_2@2%Fe_2O_3) and 24.4% for the highest amount of Fe_2O_3 (TiO_2@20%Fe_2O_3) at the surface of TiO_2 nanocrystals (Table 1).

Although the presence of iron oxide does not cause a drastic shift in the XPS peaks of O1s, it manifests itself quite differently. The deposition of Fe_2O_3 at the surface of TiO_2 nanocrystals leads to changes in the area under the O1s lines. In particular, the O_{II} component at the medium binding energy is affected. An increase in the amount of Fe_2O_3 deposited is accompanied by an increase in the fraction attributed to oxygen vacancies. For TiO_2 nanocrystals, the O_{II} fraction is equal to 34.4% and gradually increases to 38.2% for a low amount of Fe_2O_3 and up to 63.3% for a high amount of Fe_2O_3 on the surface of TiO_2. The increase in V_O contribution combined with the fact that the presence of a large amount of Fe_2O_3 results in a slight shift of the peaks can be treated as a proof of substitutional doping of Fe^{3+} into the titanium sublattice. The formation of oxygen vacancies at the surface of titanium dioxide can bring two additional electrons associated with one V_O. As a result, two Ti^{3+} ions can appear.[46]

The comparison of the optical reflectance spectra of TiO_2 before and after being covered with Fe_2O_3 is presented in Figures 5a (0.2 and 2%) and S5 (1, 10, and 20%). Figures 5b and S5b demonstrate the first derivative spectra $dR_{tot}/d\lambda$ of TiO_2, TiO_2@Fe_2O_3, and Fe_2O_3. All possible optical transitions are listed in Table S2 and shown schematically in Figure 5c.

In the case of pure TiO_2, the peak in $dR_{tot}/d\lambda$ can be seen at 3.32 eV, corresponding to anatase (1a). The same peak appears in $dR_{tot}/d\lambda$ of TiO_2@2%Fe_2O_3 at slightly different positions 3.43 eV (1a) due to the presence of iron oxide. Furthermore, four additional transitions have been identified for TiO_2@Fe_2O_3. Three of them have been assigned:

https://doi.org/10.1021/acsami.2c06404
ACS Appl. Mater. Interfaces 2022, 14, 38255−38269

- (2) at 2.9 eV—level of Fe^{3+} impurity in the forbidden band of TiO_2,[50,51]
- (4) at 2.2 eV—direct optical transition from the VB to CB in α-Fe_2O_3,
- (5) at 1.8 eV—indirect optical transition from the VB to CB in α-Fe_2O_3.[52]

In addition, a fourth transition (3) at 2.5 eV has been observed in this work when the Fe/(Fe + Ti) atomic ratio exceeded 1%. The origin of this transition remained unclear for a long time until it was realized that it could be attributed to the size effect in Fe_2O_3.[53] For nanoparticles with a size decreasing from 120 nm to 7 nm, an increase in the band gap energy from 2.18 to 2.95 eV was demonstrated. This effect has been attributed to the size effect, which was accompanied by a modification of the hematite structure. Fondell et al.[52] analyzed optical absorption as a function of film thickness for hematite. Two direct transitions were found at 2.15 and 2.45 eV, and they were blue-shifted by 0.3 and 0.45 eV, respectively, when the film thickness was decreased from 20 to 4 nm.

In the present work, structural studies do not show any evidence of phases other than α-Fe_2O_3 of iron oxide. TEM and HRTEM images for TiO_2@2%Fe_2O_3 and TiO_2@20%Fe_2O_3 composites (Figures 3, S2, and S4) confirm that iron oxide nanoparticles deposited at the surface of TiO_2 nanocrystals crystallize as α-Fe_2O_3. The combination of SEM and HRTEM studies indicates that the applied synthesis method produces relatively large 15−50 nm as well as very small 6−8 nm α-Fe_2O_3 nanoparticles on the surface of TiO_2. Therefore, we propose that the additional 2.48 eV optical transition is associated with the presence of small Fe_2O_3 nanoparticles.

3.3. Photocatalytic Degradation of RhB. RhB, as a model cationic aminoxanthene dye, is widely applied in the textile and color glass industry.[54] Its structural formula is shown in Scheme 1.

Scheme 1. Structural Formula of RhB in (a) Open and (b) Closed Forms

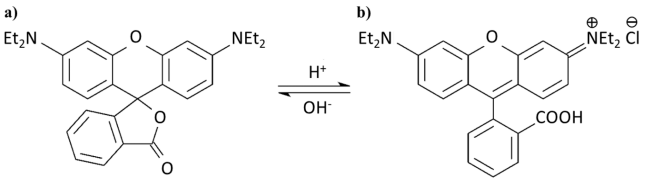

Efficient degradation of RhB is of upmost importance due to its high toxicity. There are many degradation schemes of RhB, one of them being laser cavitation.[55] The N-de-ethylation and chromophore cleavage are two degradation pathways of RhB.

In this paper, we have undertaken photocatalytic methods of dye decomposition. Under the illumination of RhB, electron transitions occur due to the presence of orbitals: HOMO (the highest occupied molecular orbital) and LUMO (the lowest unoccupied molecular orbital). For RhB, the HOMO level is at −4.97 eV and the LUMO level is at −2.73 eV relative to vacuum, giving an energy gap of 2.23 eV.[56]

Photodegradation of RhB can proceed via three oxidation routes[57,58]

$$^{\bullet}O_2^- + \text{RhB} \rightarrow H_2O + CO_2 \quad (1)$$

$$^{\bullet}OH + \text{RhB} \rightarrow H_2O + CO_2 \quad (2)$$

$$h^{\bullet} + \text{RhB} \rightarrow H_2O + CO_2 \quad (3)$$

To decide which of these three routes will play the most important role, one must consider the availability of active radicals: $^{\bullet}O_2^-$ and $^{\bullet}OH$, as well as holes and electrons in the PS. Active species are formed in the interactions of electrons e^- and holes $h^{\bullet}$ with dissolved oxygen, water, and hydrogen peroxide, according to the following reactions:[59,60]

$$O_2 + e^- \rightarrow {}^{\bullet}O_2^- \quad (4)$$

$$H_2O + h^{\bullet} \rightarrow {}^{\bullet}OH + H^+ \quad (5)$$

$$H_2O_2 + e^- \rightarrow {}^{\bullet}OH + OH^- \quad (6)$$

In PSs containing metal oxide semiconductors, electrons and holes are provided by irradiation with photons of energy $h\nu$ exceeding their band gap energy ($h\nu \geq E_g$). Oxidation and reduction abilities of the photogenerated charge carriers depend not only on the band gap of a photocatalyst but also on the proper alignment of its conduction CB and VB edges with respect to the oxidation and reduction levels of active species, as shown in Figure 6. Therefore, from the photocatalytic performance of single semiconductors or their heterojunctions, one can draw conclusions concerning their electronic structure.

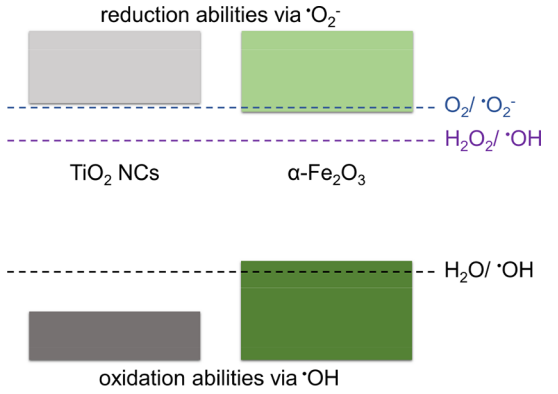

Figure 6. Energy band diagram of pure TiO_2 and Fe_2O_3.

Stoichiometric TiO_2 is a wide-band semiconductor (E_g = 3.0−3.2 eV) with CB and VB edges properly aligned with respect to the levels of oxidation and reduction of active radicals. Electrons photoexcited to the CB and holes left in the VB as a result of UV light absorption in TiO_2 can participate in reactions (eq 4) and (eq 5). The reaction (eq 6) is also possible in the presence of H_2O_2. However, visible radiation will produce an effect only in the case of defects responsible for the introduction of additional levels in the forbidden band gap of TiO_2.

On the other hand, the lower band gap of Fe_2O_3 allows visible light to generate electrons and holes. However, since CB_{Fe2O3} is located near the reduction potential of $O_2/^{\bullet}O_2^-$ (see Figure 6), electrons created under visible light in the CB of Fe_2O_3 can only reduce oxygen to superoxide radicals to a small extent.

Furthermore, the process described by eq 5 cannot occur in this oxide because its VB is above the water oxidation potential $H_2O/^{\bullet}OH$, while reduction of hydrogen peroxide (eq 6) is possible due to the CB edges being above the $H_2O_2/^{\bullet}OH$ potential. For this reason, preliminary photocatalytic studies

https://doi.org/10.1021/acsami.2c06404
ACS Appl. Mater. Interfaces 2022, 14, 38255−38269

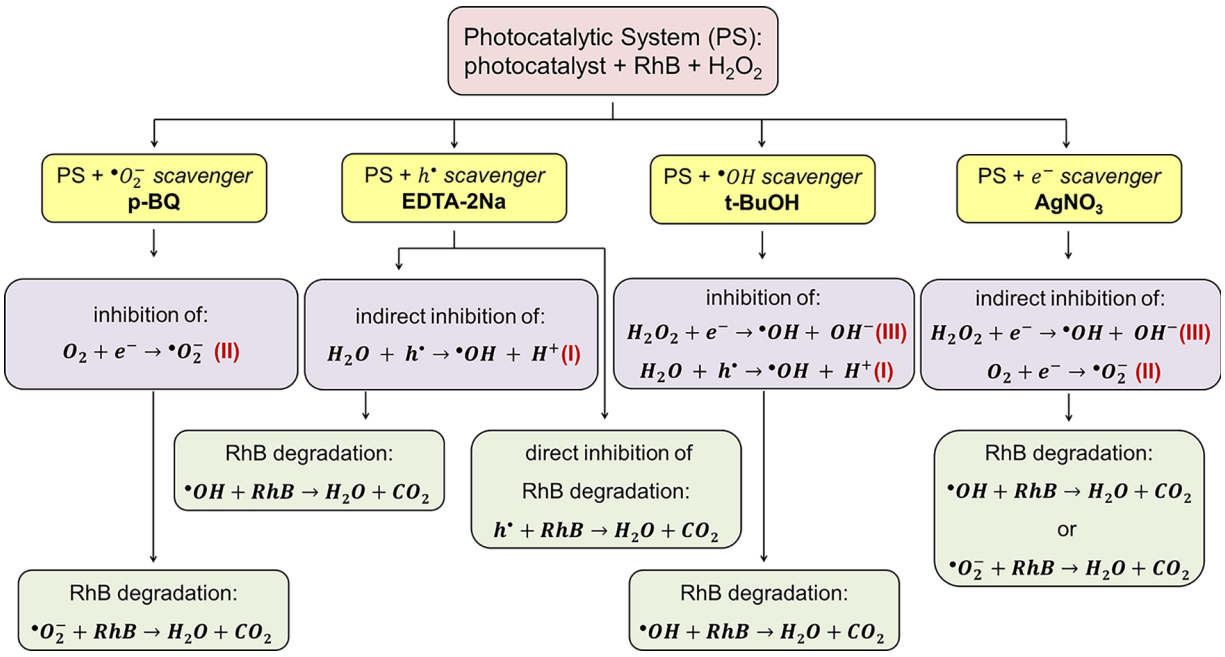

Figure 7. Schematic diagram showing the effect of the addition of particular scavengers on the mechanism of RhB decomposition.

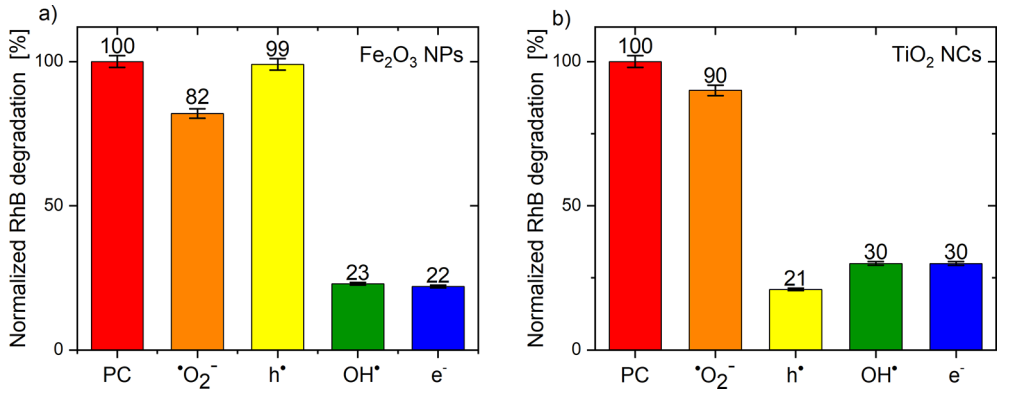

Figure 8. Effect of radical scavengers on RhB photocatalytic degradation on Fe_2O_{32} (a) and TiO_2 (b) photocatalysts under visible light.

under visible light carried out without the addition of H_2O_2 showed that dye decomposition was negligible (Figure S6a,b).

The influence of H_2O_2 addition on RhB decomposition without a photocatalyst was also investigated in the system RhB + H_2O_2 + vis (Figure S6b). The results showed no negative impact of the additive, that is, no photolysis of H_2O_2 was observed. Therefore, the rest of the photocatalytic tests were performed with its addition.

The energy band diagram presented in Figure 6 corresponds to single pure photocatalysts of TiO_2 and Fe_2O_3 treated separately. To construct the corresponding electronic model of the interface between TiO_2 and Fe_2O_3, additional well-programed experiments with scavengers of the discussed radicals were performed, as illustrated in Figure 7. A drastic decrease in the photocatalytic activity after the addition of a specific scavenger indicates that the captured radicals are the main active species in the PS. In this paper, tert-butyl alcohol (t-BuOH), disodiumethylene diaminetetraacetate (EDTA-2Na), *p*-benzoquinone (p-BQ), and $AgNO_3$ were used as $^{\bullet}OH$, $h^{\bullet}$, $^{\bullet}O_2^-$, and e^- scavengers, respectively.

The influence of scavengers on RhB decomposition is quite different for pure TiO_2 and Fe_2O_3. Figure 8 shows normalized dye degradation after 60 min from the addition of a specific scavenger in relation to degradation without its addition

$$\frac{C_o - C_{t=60\ min\ +scav.}}{C_o - C_{t=60\ min}} \bullet 100 = \frac{\text{the amount of decomposed dye with scavenger addition}}{\text{the amount of decomposed dye}}\ [\%] \quad (7)$$

The abbreviation PC in Figures 8 and 9 denotes a normalized dye degradation without the addition of scavengers; therefore, it is always equal 100%. The photocatalytic activity of hematite nanoparticles does not change after the addition of a hole scavenger (EDTA-2Na) (Figure 8a), which is consistent with the statement discussed previously (Figure 6) that VB_{Fe2O_3} is above the oxidation potential of water (reaction I does not occur, see Figure 7). The abbreviation PC in Figures 8 and 9 denotes a normalized dye degradation without the addition of scavengers; therefore, it is always equal 100%. The photocatalytic activity of hematite nanoparticles does not change after the addition of a hole scavenger (EDTA-2Na) (Figure 8a), which is consistent with the statement discussed previously (Figure 6) that VB_{Fe2O_3} is above the oxidation potential of water (reaction I does not

https://doi.org/10.1021/acsami.2c06404
ACS Appl. Mater. Interfaces 2022, 14, 38255−38269

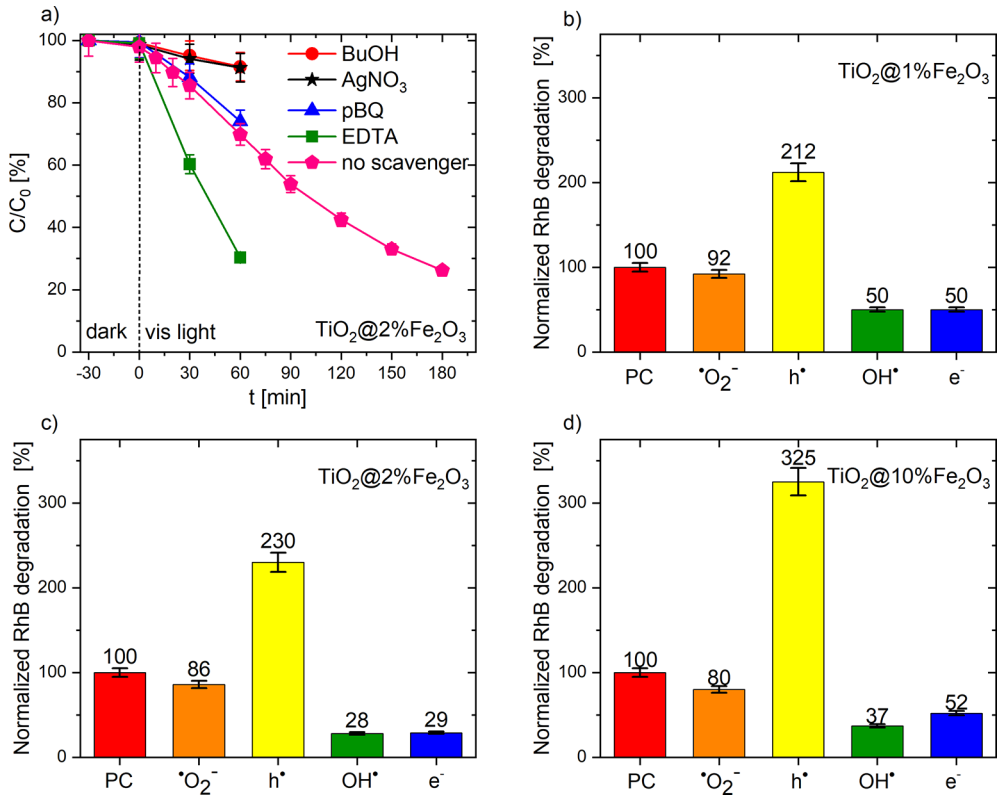

Figure 9. Effect of radical scavengers on RhB photocatalytic degradation on TiO_2@Fe_2O_3 photocatalysts under visible light: example kinetics of the dye decomposition on TiO_2@2%Fe_2O_3 (a) and normalized degradation of the dye on TiO_2@1%Fe_2O_3 (b), TiO_2@2%Fe_2O_3 (c), and TiO_2@10%Fe_2O_3 (d).

occur, see Figure 7). Furthermore, superoxide radicals have been shown to play a minor role in RhB decomposition as CB_{Fe2O3} is located only slightly higher than the $O_2/{}^{\bullet}O_2^-$ potential, which does not allow electrons to completely reduce the dissolved oxygen in the dye solution (reaction II, see Figure 7). On the other hand, a high decrease in photoactivity is observed when e^- and $OH^{\bullet}$ are captured from the system. This shows that $OH^{\bullet}$ radicals, which are formed in reaction III, play a key role in the decomposition of RhB dye (see Figure 7). After the electrons are scavenged, the reduction of H_2O_2 to $OH^{\bullet}$ is stopped, and therefore, the photocatalytic process is slower.

Different situations occur when we consider TiO_2 nanocrystals (Figure 8b). In this case, a decrease in the photocatalytic activity is observed after the addition of the e^-, $h^{\bullet}$, and $OH^{\bullet}$ scavengers. This means that the main active species, as in the case of Fe_2O_3, are hydroxyl radicals, but originating from two different reactions. First, there is the reduction of hydrogen peroxide by electrons (reaction III, see Figure 7), and second, water is oxidized by holes (reaction I, see Figure 7). Moreover, the addition of the ${}^{\bullet}O_2^-$ scavenger has little effect on photocatalysis as CB_{TiO2} is located closely to the $O_2/{}^{\bullet}O_2^-$ potential (Figure 6).

Additional changes occur in the case of a heterojunction composed of anatase nanocrystals covered with iron oxide nanoparticles (Figure 9). The p-BQ (${}^{\bullet}O_2^-$) scavenger slightly reduces the photoactivity of the tested materials. This means that in this case as well, superoxide radicals play a minor role in RhB photodegradation (Figure 9b–d). On the other hand, after scavenging the $OH^{\bullet}$ radicals and electrons from the system, a significant decrease in RhB decomposition was observed (inhibition of reaction III, see Figure 7) because the hydroxyl radicals from H_2O_2 reduction are the main active species in the decomposition of RhB. However, the most interesting effect was observed after the addition of a hole scavenger. It is assumed that the elimination of $h^{\bullet}$ from the system reduces the recombination rate, and thus, more electrons were able to reduce H_2O_2. Furthermore, it should be noted that the increase in photocatalytic activity after the addition of EDTA-2Na ($h^{\bullet}$) is proportional to the amount of Fe_2O_3 in the heterojunction (1%—212, 2%—230, and 10%—325). The small amount of hematite (TiO_2@1%Fe_2O_3) is responsible for the low area of the TiO_2@Fe_2O_3 interface where recombination can occur. When this surface increases, the number of probable recombination sites also increases; therefore, effective scavenging of holes resulted in a high increase in photoactivity in the case of TiO_2@10%Fe_2O_3 (Figures 9d and S7).

As the stability of the photocatalysts is a very important issue for practical applications, the recyclability photocatalytic tests were performed. Two selected heterostructures were subjected to the RhB photodegradation in a sequence of four successive reactions (Figure S8). After the first cycle, the efficiency of photocatalysts decreases slightly; however, in the third and fourth cycles, it remains constant. This allows us to conclude that the obtained TiO_2@Fe_2O_3 heterostructures show stability in the cyclic photocatalytic process.

4. DISCUSSION

Analysis of the spectral dependence of the absorption coefficient presented in Figures 5 and S5 shows that the presence of iron oxide Fe_2O_3 strongly modifies its shape and

https://doi.org/10.1021/acsami.2c06404
ACS Appl. Mater. Interfaces 2022, 14, 38255−38269

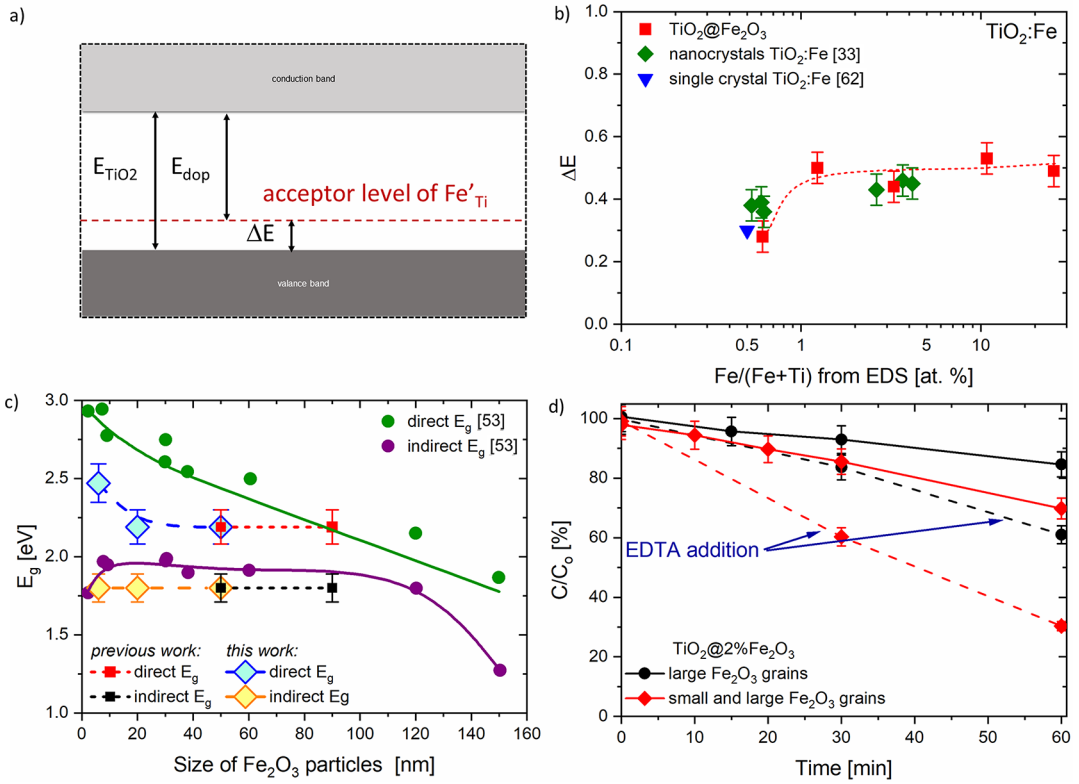

Figure 10. (a) Energy difference ΔE between the TiO_2 nanocrystal band gap E_{TiO_2} and the acceptor doping level E_{dop} as a function of the Fe/(Fe + Ti) ratio obtained from EDX, our previous work,[33] and single-crystal data from ref 62, (b) acceptor level within the TiO_2 band structure caused by Fe^{3+} doping, (c) dependence of the band gap energy E_g on the particle size of the hematite (ref 53), and (d) TiO_2@2%Fe_2O_3 nanostructure with different grain sizes of Fe_2O_3.

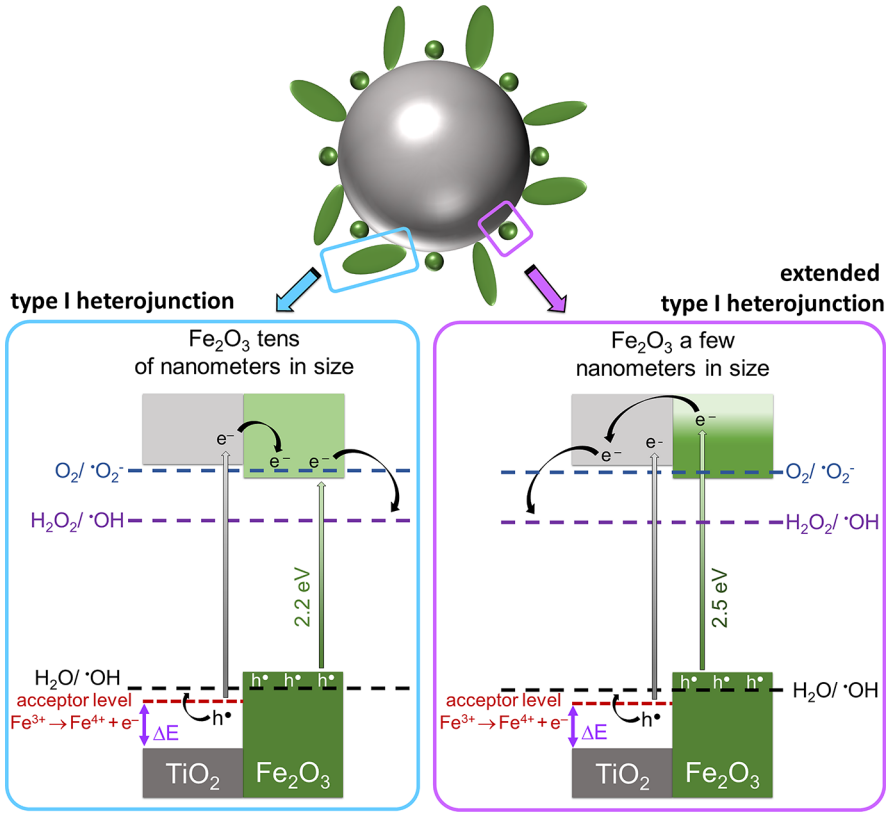

Figure 11. Proposed band diagram of the TiO_2@Fe_2O_3 heterojunction and electron as well as hole transfer routes between electronic states.

https://doi.org/10.1021/acsami.2c06404
ACS Appl. Mater. Interfaces 2022, 14, 38255−38269

moves the fundamental absorption edge from UV toward the visible range. The characteristic energies of the optical transitions in TiO_2, Fe_2O_3, and $TiO_2@Fe_2O_3$ determined as the maxima in the first derivative of $dR_{tot}/d\lambda$ are given in Table S2. The trivalent iron metal dopants Fe^{3+} can act as acceptors. The incorporation of Fe^{3+} into TiO_2 with an ionic radius (0.064 nm) smaller than that of Ti^{4+} (0.068 nm) can be expressed by the following reaction

$$Fe_2O_3 \rightarrow 2Fe'_{Ti} + V_O^{\bullet\bullet} + 3O_O \quad (8)$$

Not only optical results but also the analysis of the XPS studies support the possibility of substitution of some amount of Fe^{3+} into the titanium sublattice as Fe'_{Ti}. The energy difference ΔE between the band gap of TiO_2 nanocrystals (E_{TiO_2}) and the acceptor doping level E_{dop} (Figure 10a) was calculated from the experimental data (Table S2) and is presented as a function of Fe/(Fe + Ti) in Figure 10b. The position of the iron Fe^{3+} level within the TiO_2 band gap varies with the increasing Fe_2O_3 concentration. As can be seen, the Fe acceptor level is located in the range of 0.3−0.5 eV above the top of VB_{TiO_2} depending on the concentration of the dopants. It is also affected by the microstructural properties of titanium dioxide, that is, the form of material (nanopowders and nanocrystals) and the type of synthesis of $TiO_2@Fe_2O_3$ heterojunctions.[33,53] This effect has also been demonstrated for TiO_2 modified with chromium Cr^{3+}.[61]

The simultaneous occurrence of direct and indirect optical transitions has been demonstrated for α-Fe_2O_3,[52] as discussed in Section 3.2 of this work and illustrated in Figure 10c. The well-pronounced size effect has been reported by Chernyshova et al.[53] for direct optical transitions. The results of our studies regarding the absorption feature at 2.48 eV (3) indicate quite good correspondence with these observations (Figure 10c). This confirms that the size effect can be attributed to the presence of small 6−8 nm α-Fe_2O_3 nanograins, the evidence of which has been demonstrated by HRTEM.

The dye degradation (solid curves) presented in Figure 10d corresponds to the PS consisting of photocatalyst + RhB + H_2O_2. $TiO_2@2\%Fe_2O_3$ with different iron(III) oxide grain sizes were used as photocatalysts. It was observed that the RhB concentration for the photocatalyst with Fe_2O_3 grains of a large size decreased to 85% after 60 min, but the highest changes equal to 70% were observed for the $TiO_2@2\%Fe_2O_3$ heterojunction composed of both the large and small Fe_2O_3 grains after the same time. The explanation of this phenomenon is related to the different band structure at the interface caused by the different microstructure (see the explanation of Figure 11). Furthermore, when the hole scavenger was added (dashed lines, see Figure 10d), the decomposition accelerated due to the reduction of recombination at the $TiO_2@Fe_2O_3$ interface (from 70 to 30% in the case of $TiO_2@2\%Fe_2O_3$).

Based on the experimental results, including optical, structural, and electronic properties, as well as HRTEM imaging, it was possible to propose the energy diagrams of the $TiO_2@Fe_2O_3$ heterostructure presented in Figure 11 and the mechanism of RhB decomposition.

Covering of titanium dioxide with iron oxide is claimed to result in the formation of an additional acceptor level within the TiO_2 band gap. Upon visible light irradiation, generation of electron−hole pairs can occur in TiO_2 only when the acceptor level is activated (2.80 eV). Electrons excited from the Fe^{3+} level are transferred to the TiO_2 CB following the reaction: $Fe^{3+} \rightarrow Fe^{4+} + e'$. Centers Fe^{4+} can be treated as Fe^{3+} ions with photoholes $h^{\bullet}$ located on them. The holes can move in the TiO_2 lattice by the hopping mechanism according to the reaction $Fe^{4+} \rightarrow Fe^{3+} + h^{\bullet}$. The position of the Fe acceptor level is below the water oxidation potential $H_2O/^{\bullet}OH$, while water oxidizes to hydroxyl radicals (eq 5) and then $^{\bullet}OH_{(H_2O)}$ participates in RhB degradation (eq 2). However, it is a subsidiary reaction in this system.

In the previous work, hematite grains tens of nanometers in size, characterized by a direct band gap of 2.2 eV, formed at the TiO_2 surface, and the type I heterojunction was created (Figure 11a). Furthermore, in this work, the obtained $TiO_2@Fe_2O_3$ heterojunction possesses the same large Fe_2O_3 grains, but here, this interface has been carefully examined. In the type I heterojunction, the photoelectrons involved in the RhB decomposition originated from two sources. The first is the acceptor level formed in TiO_2, from which the excited e^- are transferred to the CB of TiO_2 and then to Fe_2O_3. The second are photoelectrons that form in the iron oxide (2.2 eV). Both participate in the reduction of hydrogen peroxide to $OH^{\bullet}$, and a small part of them reduced O_2 to $^{\bullet}O_2^-$. As mentioned in Section 3.3, hydroxyl radicals are the main active species in RhB degradation.

The extended type I heterojunction is created because of an additional optical transition at a photon energy of 2.5 eV that originated from Fe_2O_3 nanoparticles with a size of several nanometers. Photoelectrons from high energy levels in iron(III) oxide are transferred to lower energy states in the CB of titanium dioxide through the interface. Then, together with the electrons from TiO_2, they reduce H_2O_2 to $OH^{\bullet}$, which is the main route of the decomposition of RhB.

5. CONCLUSIONS

The $TiO_2@Fe_2O_3$ heterostructures composed of shape-controlled titanium dioxide nanocrystals covered with α-Fe_2O_3 nanoparticles have been successfully synthesized. The results of various characterization methods have shown that in addition to the presence of iron oxide nanoparticles on the surface of TiO_2, the TiO_2 lattice is substitutionally doped with Fe^{3+} ions, which is accompanied by the formation of oxygen vacancies. First, XPS studies of the O1peak have confirmed the existence of the component attributed to the oxygen vacancies V_O in the TiO_2 lattice. Furthermore, the formation of a thin, doped TiO_2:Fe layer has been found, manifested by the appearance of an additional acceptor level within the TiO_2 band gap. In terms of the microstructure, SEM analysis revealed α-Fe_2O_3 nanoparticles of different shapes agglomerated in irregular grains up to 100 nm in size. However, deposition on the surface of TiO_2 nanocrystals causes the crystallization of evenly distributed Fe_2O_3 nanoparticles with sizes several tens of nanometers (up to 50 nm from SEM) and a few nanometers (6−8 nm from HRTEM). The presence of Fe_2O_3 nanoparticles in $TiO_2@Fe_2O_3$ heterostructures has also been evident in UV−vis studies, which have also shown an additional optical transition attributed to the size effect of α-Fe_2O_3. The photocatalytic performance of the TiO_2 nanocrystals and heterostructures of $TiO_2@Fe_2O_3$ toward RhB decomposition and the detailed mechanism of this reaction have been investigated using relevant scavengers to determine active species in the system. In-depth analysis has allowed the indication of $^{\bullet}OH$ hydroxyl radicals as the main active species

https://doi.org/10.1021/acsami.2c06404
ACS Appl. Mater. Interfaces 2022, 14, 38255−38269

responsible for the decomposition of RhB by TiO_2 nanocrystals, Fe_2O_3 nanoparticles, and TiO_2@Fe_2O_3 heterojunctions. On the basis of the experimental results and the relative band positions of the TiO_2@Fe_2O_3 materials, the mechanism of RhB degradation was proposed. Under visible light, in addition to Fe_2O_3, only the Fe^{3+} acceptor level within the TiO_2 band gap is active, and electron−hole pairs are created. Electrons excited from the Fe^{3+} acceptor level are transferred to the TiO_2 CB. Furthermore, the high energy levels located in the Fe_2O_3 CB associated with the optical transition are responsible for the electron transfer from CB_{Fe2O3} to CB_{TiO2}. Therefore, all electrons in the TiO_2 CB participate in the formation of OH radicals in the reaction with H_2O_2, which is considered the most probable route of RhB decomposition. The proposed band diagram of the TiO_2@Fe_2O_3 heterojunction supports the hypothesis of an extended type I band configuration.

■ ASSOCIATED CONTENT

Supporting Information

The Supporting Information is available free of charge at https://pubs.acs.org/doi/10.1021/acsami.2c06404.

EDX analysis of chemical composition; XRD pattern of the TiO_2 nanocrystal; TEM images of the TiO_2@Fe_2O_3 heterostructure; EDX mapping and HRTEM images with FFT and IFFT analysis of the TiO_2@Fe_2O_3 heterostructure; XPS analysis of the TiO_2@Fe_2O_3 heterostructure; analysis of spectral dependence of total reflectance and optical transition energies of TiO_2 and the TiO_2@Fe_2O_3 heterostructure; analysis of photocatalytic decomposition of RhB dye under visible radiation, photocatalytic activity with and without the addition of H_2O_2 to the PS; dye degradation in the presence of scavenger of holes; and recycled photocatalytic decomposition process of RhB in the presence of TiO_2@Fe_2O_3 and H_2O_2 (PDF)

■ AUTHOR INFORMATION

Corresponding Authors

Anita Trenczek-Zajac − *Faculty of Materials Science and Ceramics, AGH University of Science and Technology, Krakow 30-059, Poland;* orcid.org/0000-0002-2742-0748; Email: anita.trenczek-zajac@agh.edu.pl

Milena Synowiec − *Faculty of Materials Science and Ceramics, AGH University of Science and Technology, Krakow 30-059, Poland;* orcid.org/0000-0002-7589-6169; Email: milsyn@agh.edu.pl

Authors

Katarzyna Zakrzewska − *Faculty of Computer Science, Electronics and Telecommunications, AGH University of Science and Technology, Krakow 30-059, Poland*

Karolina Zazakowny − *Faculty of Materials Science and Ceramics, AGH University of Science and Technology, Krakow 30-059, Poland*

Kazimierz Kowalski − *Faculty of Metals Engineering and Industrial Computer Science, AGH University of Science and Technology, Krakow 30-059, Poland*

Andrzej Dziedzic − *Institute of Physics, College of Natural Sciences, University of Rzeszow, Rzeszow 35-310, Poland;* orcid.org/0000-0002-4116-3100

Marta Radecka − *Faculty of Materials Science and Ceramics, AGH University of Science and Technology, Krakow 30-059, Poland*

Complete contact information is available at: https://pubs.acs.org/10.1021/acsami.2c06404

Notes

The authors declare no competing financial interest.

■ ACKNOWLEDGMENTS

This research project was supported by the program "Excellence initiative—research university" for the AGH University of Science and Technology.

■ REFERENCES

(1) Patra, A. K.; Dutta, A.; Bhaumik, A. Highly Ordered Mesoporous TiO_2-Fe_2O_3 Mixed Oxide Synthesized by Sol-Gel Pathway: An Efficient and Reusable Heterogeneous Catalyst for Dehalogenation Reaction. *ACS Appl. Mater. Interfaces* **2012**, *4*, 5022−5028.

(2) Xia, Y.; Yin, L. Core-shell Structured α-Fe_2O_3@TiO_2 Nanocomposites with Improved Photocatalytic Activity in the Visible Light Region. *Phys. Chem. Chem. Phys.* **2013**, *15*, 18627−18634.

(3) Yao, K.; Basnet, P.; Sessions, H.; Larsen, G. K.; Murph, S. E. H.; Zhao, Y. Fe_2O_3-TiO_2 Core-Shell Nanorod Arrays for Visible Light Photocatalytic Applications. *Catal. Today* **2016**, *270*, 51−58.

(4) Li, X.; Lin, H.; Chen, X.; Niu, H.; Liu, J.; Zhang, T.; Qu, F. Dendritic α-Fe_2O_3/TiO_2 nanocomposites with improved visible light photocatalytic activity. *Phys. Chem. Chem. Phys.* **2016**, *18*, 9176−9185.

(5) Mendiola-Alvarez, S. Y.; Hernández-Ramírez, A.; Guzmán-Mar, J. L.; Maya-Treviño, M. L.; Caballero-Quintero, A.; Hinojosa-Reyes, L. A novel P-doped Fe_2O_3-TiO_2 Mixed Oxide: Synthesis, Characterization and Photocatalytic Activity under Visible Radiation. *Catal. Today* **2019**, *328*, 91−98.

(6) Wannapop, S.; Somdee, A.; Bovornratanaraks, T. Experimental Study of Thin Film Fe_2O_3/TiO_2 for Photocatalytic Rhodamine B Degradation. *Inorg. Chem. Commun.* **2021**, *128*, 108585.

(7) Li, L.; Zhang, J.; Zhu, Q. A Novel Fractional Crystallization Route to Porous TiO_2-Fe_2O_3 Composites: Large Scale Preparation and High Performances as a Photocatalyst and Li-ion Battery Anode. *Dalton Trans.* **2016**, *45*, 2888−2896.

(8) Yang, J.; Wu, Q.; Yang, X.; He, S.; Khan, J.; Meng, Y.; Zhu, X.; Tong, S.; Wu, M. Chestnut-Like TiO_2@α-Fe_2O_3 Core-Shell Nanostructures with Abundant Interfaces for Efficient and Ultralong Life Lithium-Ion Storage. *ACS Appl. Mater. Interfaces* **2017**, *9*, 354−361.

(9) Lou, Z.; Li, F.; Deng, J.; Wang, L.; Zhang, T. Branch-like Hierarchical Heterostructure (α-Fe_2O_3/TiO_2): A Novel Sensing Material for Trimethylamine Gas Sensor. *ACS Appl. Mater. Interfaces* **2013**, *5*, 12310−12316.

(10) Zhu, C. L.; Yu, H. L.; Zhang, Y.; Wang, T. S.; Ouyang, Q. Y.; Qi, L. H.; Chen, Y. J.; Xue, X. Y. Fe_2O_3/TiO_2 Tube-like Nanostructures: Synthesis, Structural Transformation and the Enhanced Sensing Properties. *ACS Appl. Mater. Interfaces* **2012**, *4*, 665−671.

(11) Yang, J. S.; Lin, W. H.; Lin, C. Y.; Wang, B. S.; Wu, J. J. N-Fe_2O_3 to N^+-TiO_2 Heterojunction Photoanode for Photoelectrochemical Water Oxidation. *ACS Appl. Mater. Interfaces* **2015**, *7*, 13314−13321.

(12) Sołtys-Mróz, M.; Syrek, K.; Pierzchała, J.; Wiercigroch, E.; Malek, K.; Sulka, G. D. Band Gap Engineering of Nanotubular Fe_2O_3-TiO_2 Photoanodes by Wet Impregnation. *Appl. Surf. Sci.* **2020**, *517*, 146195.

(13) Baldovi, H. G. Optimization of α-Fe_2O_3 Nanopillars Diameters for Photoelectrochemical Enhancement of α-Fe_2O_3-TiO_2 Heterojunction. *Nanomaterials* **2021**, *11*, 2019.

(14) Schneider, J.; Matsuoka, M.; Takeuchi, M.; Zhang, J.; Horiuchi, Y.; Anpo, M.; Bahnemann, D. W. Understanding TiO_2 Photocatalysis: Mechanisms and Materials. *Chem. Rev.* **2014**, *114*, 9919−9986.
(15) Kontos, A. I.; Kontos, A. G.; Tsoukleris, D. S.; Bernard, M. C.; Spyrellis, N.; Falaras, P. Nanostructured TiO_2 Films for DSSCS Prepared by Combining Doctor-Blade and Sol-Gel Techniques. *J. Mater. Process. Technol.* **2008**, *196*, 243−248.
(16) Euvananont, C.; Junin, C.; Inpor, K.; Limthongkul, P.; Thanachayanont, C. TiO_2 Optical Coating Layers for Self-Cleaning Applications. *Ceram. Int.* **2008**, *34*, 1067−1071.
(17) Lin, S.; Li, D.; Wu, J.; Li, X.; Akbar, S. A. A Selective Room Temperature Formaldehyde Gas Sensor using TiO_2 Nanotube Arrays. *Sens. Actuators, B* **2011**, *156*, 505−509.
(18) Mishra, M.; Chun, D. M. α-Fe_2O_3 as a Photocatalytic Material: A Review. *Appl. Catal., A* **2015**, *498*, 126−141.
(19) Zhang, J.; Kuang, M.; Wang, J.; Liu, R.; Xie, S.; Ji, Z. Fabrication of Carbon Quantum Dots/TiO_2/Fe_2O_3 Composites and Enhancement of Photocatalytic Activity under Visible Light. *Chem. Phys. Lett.* **2019**, *730*, 391−398.
(20) Li, J.; Wu, N. Semiconductor-Based Photocatalysts and Photoelectrochemical Cells for Solar Fuel Generation: A Review. *Catal. Sci. Technol.* **2015**, *5*, 1360−1384.
(21) Corby, S.; Rao, R. R.; Steier, L.; Durrant, J. R. The Kinetics of Metal Oxide Photoanodes from Charge Generation to Catalysis. *Nat. Rev. Mater.* **2021**, *6*, 1136−1155.
(22) Low, J.; Yu, J.; Jaroniec, M.; Wageh, S.; Al-Ghamdi, A. A. Heterojunction Photocatalysts. *Adv. Mater.* **2017**, *29*, 1601694.
(23) Bootluck, W.; Chittrakarn, T.; Techato, K.; Jutaporn, P.; Khongnakorn, W. S-Scheme α-Fe_2O_3/TiO_2 Photocatalyst with Pd Cocatalyst for Enhanced Photocatalytic H_2 Production Activity and Stability. *Catal. Lett.* **2021**, DOI: 10.1007/s10562-021-03873-5.
(24) Yang, X.; Liu, R.; Du, C.; Dai, P.; Zheng, Z.; Wang, D. Improving Hematite-Based Photoelectrochemical Water Splitting with Ultrathin TiO_2 by Atomic Layer Deposition. *ACS Appl. Mater. Interfaces* **2014**, *6*, 12005−12011.
(25) Li, X.; Bassi, P. S.; Boix, P. P.; Fang, Y.; Wong, L. H. Revealing the Role of TiO_2 Surface Treatment of Hematite Nanorods Photoanodes for Solar Water Splitting. *ACS Appl. Mater. Interfaces* **2015**, *7*, 16960−16966.
(26) Wang, J.; Feng, B.; Su, J.; Guo, L. Enhanced Bulk and Interfacial Charge Transfer Dynamics for Efficient Photoelectrochemical Water Splitting: The Case of Hematite Nanorod Arrays. *ACS Appl. Mater. Interfaces* **2016**, *8*, 23143−23150.
(27) Kodan, N.; Agarwal, K.; Mehta, B. R. All-Oxide α-Fe_2O_3/H:TiO_2 Heterojunction Photoanode: A Platform for Stable and Enhanced Photoelectrochemical Performance through Favorable Band Edge Alignment. *J. Phys. Chem. C* **2019**, *123*, 3326−3335.
(28) Mei, Q.; Zhang, F.; Wang, N.; Yang, Y.; Wu, R.; Wang, W. TiO_2/Fe_2O_3 Heterostructures with Enhanced Photocatalytic Reduction of Cr(VI) under Visible Light Irradiation. *RSC Adv.* **2019**, *9*, 22764−22771.
(29) Huang, R.; Liang, R.; Fan, H.; Ying, S.; Wu, L.; Wang, X.; Yan, G. Enhanced Photocatalytic Fuel Denitrification over TiO_2/α-Fe_2O_3 Nanocomposites under Visible Light Irradiation. *Sci. Rep.* **2017**, *7*, 7858.
(30) Liu, C.; Tong, R.; Xu, Z.; Kuang, Q.; Xie, Z.; Zheng, L. Efficiently enhancing the photocatalytic activity of faceted TiO_2 nanocrystals by selectively loading α-Fe_2O_3 and Pt co-catalysts. *RSC Adv.* **2016**, *6*, 29794−29801.
(31) Tada, H.; Jin, Q.; Iwaszuk, A.; Nolan, M. Molecular-Scale Transition Metal Oxide Nanocluster Surface-Modified Titanium Dioxide as Solar-Activated Environmental Catalysts. *J. Phys. Chem. C* **2014**, *118*, 12077−12086.
(32) Wang, T.; Yang, G.; Liu, J.; Yang, B.; Ding, S.; Yan, Z.; Xiao, T. Orthogonal Synthesis, Structural Characteristics, and Enhanced Visible-Light Photocatalysis of Mesoporous Fe_2O_3/TiO_2 Heterostructured Microspheres. *Appl. Surf. Sci.* **2014**, *311*, 314−323.
(33) Synowiec, M.; Micek-Ilnicka, A.; Szczepanowicz, K.; Różycka, A.; Trenczek-Zajac, A.; Zakrzewska, K.; Radecka, M. Functionalized Structures Based on Shape-Controlled TiO_2. *Appl. Surf. Sci.* **2019**, *473*, 603−613.
(34) Peng, L.; Xie, T.; Lu, Y.; Fan, H.; Wang, D. Synthesis, Photoelectric Properties and Photocatalytic Activity of the Fe_2O_3/TiO_2 Heterogeneous Photocatalysts. *Phys. Chem. Chem. Phys.* **2010**, *12*, 8033.
(35) Liu, J.; Yang, S.; Wu, W.; Tian, Q.; Cui, S.; Dai, Z.; Ren, F.; Xiao, X.; Jiang, C. 3D Flowerlike α-Fe_2O_3@TiO_2 Core-Shell Nanostructures: General Synthesis and Enhanced Photocatalytic Performance. *ACS Sustainable Chem. Eng.* **2015**, *3*, 2975−2984.
(36) Tao, Q.; Huang, X.; Bi, J.; Wei, R.; Xie, C.; Zhou, Y.; Yu, L.; Hao, H.; Wang, J. Aerobic Oil-Phase Cyclic Magnetic Adsorption to Synthesize 1D Fe_2O_3@TiO_2 Nanotube Composites for Enhanced Visible-Light Photocatalytic Degradation. *Nanomaterials* **2020**, *10*, 1345.
(37) Barreca, D.; Carraro, G.; Warwick, M. E. A.; Kaunisto, K.; Gasparotto, A.; Gombac, V.; Sada, C.; Turner, S.; Van Tendeloo, G.; Maccato, C.; et al. Fe_2O_3-TiO_2 Nanosystems by a Hybrid PE-CVD/ALD Approach: Controllable Synthesis, Growth Mechanism, and Photocatalytic Properties. *CrystEngComm* **2015**, *17*, 6219−6226.
(38) Tilgner, D.; Friedrich, M.; Verch, A.; de Jonge, N.; Kempe, R. A Metal-Organic Framework Supported Nonprecious Metal Photocatalyst for Visible-Light-Driven Wastewater Treatment. *ChemPhotoChem* **2018**, *2*, 349−352.
(39) Jia, M.; Yang, Z.; Xiong, W.; Cao, J.; Xiang, Y.; Peng, H.; Jing, Y.; Zhang, C.; Xu, H.; Song, P. Magnetic Heterojunction of Oxygen-deficient Ti^{3+}-TiO_2 and Ar-Fe_2O_3 Derived from Metal-organic Frameworks for Efficient Peroxydisulfate (PDS) Photo-activation. *Appl. Catal., B* **2021**, *298*, 120513.
(40) Cao, Y.; Yang, W.; Zhang, W.; Liu, G.; Yue, P. Improved Photocatalytic Activity of Sn^{4+} Doped TiO_2 Nanoparticulate Films Prepared by Plasma-Enhanced Chemical Vapor Deposition. *New J. Chem.* **2004**, *28*, 218.
(41) Ohsaka, T.; Izumi, F.; Fujiki, Y. Raman Spectrum of Anatase, TiO_2. *J. Raman Spectrosc.* **1978**, *7*, 321−324.
(42) Mansour, H.; Letifi, H.; Bargougui, R.; De Almeida-Didry, S.; Negulescu, B.; Autret-Lambert, C.; Gadri, A.; Ammar, S. Structural, Optical, Magnetic and Electrical Properties of Hematite (α-Fe_2O_3) Nanoparticles Synthesized by Two Methods: Polyol and Precipitation. *Appl. Phys. A: Mater. Sci. Process.* **2017**, *123*, 10.
(43) Bersani, D.; Lottici, P. P.; Montenero, A. Micro-Raman Investigation of Iron Oxide Films and Powders Produced by Sol-Gel Syntheses. *J. Raman Spectrosc.* **1999**, *30*, 355−360.
(44) Ali, T.; Tripathi, P.; Azam, A.; Raza, W.; Ahmed, A. A. S.; Ahmed, A. A. S.; Muneer, M. Photocatalytic Performance of Fe-doped TiO_2 Nanoparticles under Visible-light Irradiation. *Mater. Res. Express* **2017**, *4*, 015022.
(45) Saha, N. C.; Tompkins, H. G. Titanium Nitride Oxidation Chemistry: An X-ray Photoelectron Spectroscopy Study. *J. Appl. Phys.* **1992**, *72*, 3072−3079.
(46) Ghobadi, A.; Ulusoy, T. G.; Garifullin, R.; Guler, M. O.; Okyay, A. K. A Heterojunction Design of Single Layer Hole Tunneling ZnO Passivation Wrapping around TiO_2 Nanowires for Superior Photocatalytic Performance. *Sci. Rep.* **2016**, *6*, 30587.
(47) Bajnóczi, É.G.; Balázs, N.; Mogyorósi, K.; Srankó, D. F.; Pap, Z.; Ambrus, Z.; Canton, S. E.; Norén, K.; Kuzmann, E.; Vértes, A.; et al. The Influence of the Local Structure of Fe(III) on the Photocatalytic Activity of Doped TiO_2 Photocatalysts-An EXAFS, XPS and Mössbauer Spectroscopic Study. *Appl. Catal., B* **2011**, *103*, 232−239.
(48) Yamashita, T.; Hayes, P. Analysis of XPS Spectra of Fe^{2+} and Fe^{3+} Ions in Oxide Materials. *Appl. Surf. Sci.* **2008**, *254*, 2441−2449.
(49) Moradi, V.; Jun, M. B. G.; Blackburn, A.; Herring, R. A. Significant Improvement in Visible Light Photocatalytic Activity of Fe Doped TiO_2 Using an Acid Treatment Process. *Appl. Surf. Sci.* **2018**, *427*, 791−799.
(50) Li, J.-Q.; Wang, D.-F.; Guo, Z.-Y.; Zhu, Z.-F. Preparation, Characterization and Visible-light-driven Photocatalytic Activity of

Fe-incorporated TiO_2 Microspheres Photocatalysts. *Appl. Surf. Sci.* **2012**, *263*, 382−388.
(51) Santos, R. D. S.; Faria, G. A.; Giles, C.; Leite, C. A. P.; Barbosa, H. D. S.; Arruda, M. A. Z.; Longo, C. Iron Insertion and Hematite Segregation on Fe-Doped TiO_2 Nanoparticles Obtained from Sol-Gel and Hydrothermal Methods. *ACS Appl. Mater. Interfaces* **2012**, *4*, 5555−5561.
(52) Fondell, M.; Jacobsson, T. J.; Boman, M.; Edvinsson, T. Optical Quantum Confinement in Low Dimensional Hematite. *J. Mater. Chem. A* **2014**, *2*, 3352−3363.
(53) Chernyshova, I. V.; Ponnurangam, S.; Somasundaran, P. On the Origin of an Unusual Dependence of (Bio)chemical Reactivity of Ferric Hydroxides on Nanoparticle Size. *Phys. Chem. Chem. Phys.* **2010**, *12*, 14045.
(54) Liang, L.; Cheng, L.; Zhang, Y.; Wang, Q.; Wu, Q.; Xue, Y.; Meng, X. Efficiency and Mechanisms of Rhodamine B Degradation in Fenton-like Systems based on Zero-valent Iron. *RSC Adv,* **2020**, *10*, 28509−28515.
(55) Gu, J.; Luo, C.; Zhou, W.; Tong, Z.; Zhang, H.; Zhang, P.; Ren, X. Degradation of Rhodamine B in Aqueous Solution by Laser Cavitation. *Ultrason. Sonochem.* **2020**, *68* (68), 105181.
(56) Zhao, H.; Zhang, Y.; Li, G.; Tian, F.; Tang, H.; Chen, R. Rhodamine B-sensitized BiOCl Hierarchical a Nanostructure for Methyl Orange Photodegradation. *RSC Adv.* **2016**, *6*, 7772−7779.
(57) Chengjie, S.; Mingshan, F.; Bo, H.; Tianjun, C.; Liping, W.; Weidong, S. Synthesis of a g-C_3N_4-sensitized and $NaNbO_3$-substrated II-type Heterojunction with Enhanced Photocatalytic Degradation Activity. *CrystEngComm* **2015**, *17*, 4575−4583.
(58) Carneiro, J. O.; Samantilleke, A. P.; Parpot, P.; Fernandes, F.; Pastor, M.; Correia, A.; Luís, E. A.; Chivanga Barros, A. A.; Teixeira, V. Visible Light Induced Enhanced Photocatalytic Degradation of Industrial Effluents (Rhodamine B) in Aqueous Media Using TiO_2 Nanoparticles. *J. Nanomater.* **2016**, *2016*, 1−13.
(59) Yao, T.; Shi, L.; Wang, H.; Wang, F.; Wu, J.; Zhang, X.; Sun, J.; Cui, T. A Simple Method for the Preparation of TiO_2/Ag-AgCl@ Polypyrrole Composite and Its Enhanced Visible-Light Photocatalytic Activity. *Chem.—Asian J.* **2016**, *11*, 141−147.
(60) Nosaka, Y.; Nosaka, A. Y. Generation and Detection of Reactive Oxygen Species in Photocatalysis. *Chem. Rev.* **2017**, *117*, 11302−11336.
(61) Kollbek, K.; Sikora, M.; Kapusta, C.; Szlachetko, J.; Radecka, M.; Lyson-Sypien, B.; Zakrzewska, K. Incorporation of Chromium into TiO_2 Nanopowders. *Mater. Res. Bull.* **2015**, *64*, 112−116.
(62) Radecka, M.; Rekas, M.; Zakrzewska, K. Electrical and Optical Properties of Undoped and Fe-Doped TiO_2 Single Crystals. *Solid State Phenom.* **1994**, *39*−*40*, 113−116.

https://doi.org/10.1021/acsami.2c06404
ACS Appl. Mater. Interfaces 2022, 14, 38255−38269